Journal of The Electrochemical Society

The Electrochemical Society
Advancing solid state & electrochemical science & technology

OPEN ACCESS

Understanding the Failure Mode of Electroless Nickel Immersion Gold Process: In Situ-Raman Spectroscopy and Electrochemical Characterization

To cite this article: Alessandra Accogli *et al* 2020 *J. Electrochem. Soc.* **167** 082507

Journal of The Electrochemical Society, 2020 **167** 082507

Understanding the Failure Mode of Electroless Nickel Immersion Gold Process: In Situ-Raman Spectroscopy and Electrochemical Characterization

Alessandra Accogli,[1,*] Eugenio Gibertini,[1] Gabriele Panzeri,[1,*] Andrea Lucotti,[2] and Luca Magagnin[1,,z]**

[1]*Department of Chemistry, Materials and Chemical Engineering Giulio Natta, Politecnico di Milano, 20131 Milano, Italy*
[2]*Department of Chemistry, Materials and Chemical Engineering Giulio Natta, Politecnico di Milano, 20133 Milano, Italy*

Since the early 70s, printed circuit boards (PCBs) are firmly entrenched in all electronic branches, from the consumer electronics to scientific and medical equipment, culminating later in the personal computer industry. Electroless nickel immersion gold (ENIG) process is one of the most used selective finishing in PCBs production. It involves two different electroless deposition mechanisms: (1) NiP autocatalytic deposition and (2) gold galvanic immersion plating in which displacement reactions are involved. Because during ENIG process, NiP is dissolved from the electrode surface into the solution, it can be considered as a controlled corrosion process of the metal substrate: selection of the complexing agents in solution is thus crucial. Since they are the most used complexing agents, EDTA and citric acid have been investigated. In order to understand their effects on the NiP surface during the immersion plating, open circuit potential (V_{oc}) and linear sweep voltammetry (LSV) measurements have been performed. Furthermore, to establish which complexes are adsorbed on the electrode surface during the plating process, in situ Raman spectroscopy was carried out showing EDTA to be the most effective Ni cations chelating agent. To assess the effect of Cu contamination, accountable of reddish gold failure mode, the electrochemical and in situ spectroscopic analyses on both immersion gold solution and polluted revealed that the adsorption of $Cu(CN)_2^-$ and/or $Cu(CN)_3^{2-}$ complexes is competitive with $Au(CN)_2^-$. To evaluate the effects of copper contamination on gold nucleation and growth FE-SEM and AFM were carried out, while gold layer solderability has been evaluated according to NF-A-89 400 standard.
 [DOI: 10.1149/1945-7111/ab8ce6]

Manuscript submitted March 3, 2020; revised manuscript received April 16, 2020. Published May 5, 2020. *This was paper 1538 presented at the Honolulu, Hawaii, Meeting of the Society, October 2–7, 2016.*

Supplementary material for this article is available online

Printed circuit boards (PCBs) constitute a very important strategic component for electronic products and are likely to continue to be the icon of the electronic industry, counting about $1 trillion selling in electronic equipment each year.[1–3] The use of PCBs ensures a high level of repeatability and, if properly produced, they offer uniformity of electrical characteristics. This means that the PCBs production process, especially in terms of surface finishing selection, has to be properly characterized and understood in order to enhance the properties of the metallization for better component performances. In the electronic industry, the Electroless Nickel Immersion Gold (ENIG) process is one of the most used selective finish for PCB production. Although it is one of the most expensive process requiring a high number of steps, it allows to obtain a very smooth surface and a high compatibility with a wide range of components assembly methods, especially in case of lead-free solders. Furthermore, because ENIG finish is based on precious metal, it provides high corrosion resistance, excellent wettability and conductivity, and long storage time for boards.[4] The ENIG process consists of a series of unitary and separate processes, from the substrate acid cleaning and activation to the electroless nickel deposition and immersion gold plating. In this particular case, electroless nickel deposition is an autocatalytic process on palladium-activated copper substrate in which Ni is typically co-deposited with phosphorous in an amount comprising in 6%–8% by weight using a chemical reducing agent, e.g. hydrated sodium hypophosphite $NaPO_2H_2{\cdot}H_2O$, dissolved in solution. Because electroless plating occurs simply by wetting the catalytic metal surface in solution, a remarkable degree of uniformity is achieved.[5–8] In case of PCB, NiP metal layer is necessary to protect Cu lines from quick oxidation to guarantee good corrosion resistance and mechanical properties. To prevent the oxidation of Ni surface and to assure better conductivity, a gold layer is deposited simply immerging the NiP layers in the suitable solution. The ENIG process involves galvanic displacement reaction in which Ni atoms dissolve from the substrate into the solution while gold ions are reduced on the electroless nickel substrate.[9] The overall process can be seen as a combination of two simultaneous electrochemical reactions driven by the potential difference between anodic and cathodic processes. In a simplified manner, the process can be described as follows:

Anodic Reaction:

$$Ni \rightarrow Ni^{2+} + 2e^-$$
$$E_{Ni^{2+}/Ni} = -0.275\ V \text{ vs SHE}$$

Cathodic Reaction:

$$Au^+ + e^- \rightarrow Au^0$$
$$E_{Au^+/Au} = 1.692\ V \text{ vs SHE}$$

Overall Reaction:

$$Ni + 2Au^+ \rightarrow Ni^{2+} + 2Au^0$$

Although the ENIG process is an attractive and interesting finishing, the process often suffers, especially in the real industrial applications, of a problem known as black pad, responsible for mechanical failure of solder joints.[4,10,11] Several efforts have been done in order to understand the causes of this defect and how to prevent it. Usually, it may be causes by differences of surface potential induced by plating parameters, bath chemical composition and contaminations and pads connection that can induce a non-uniform gold layer deposition affecting the properties of the board both in terms of surface appearance and solderability.[4,10–15] This effect, known as galvanic effect, responsible of Ni layer hypercorrosion, is strongly dependent both by the surface preparation, inducing Cu contamination during the IG step, and by chemical species adsorbed on the surface, deeply affecting the gold deposition rate.[4,10,11,16,17] In particular, Au

*Electrochemical Society Student Member.
**Electrochemical Society Member.
[z]E-mail: luca.magagnin@polimi.it

ions tend to be easily reduced on more cathodic surface with respect to the less cathodic one, resulting in higher deposition rate and more thicker gold layer. Very often, these differences in gold deposition rates correspond to different metallic appearance: extremely fast Au deposition could lead to reddish gold coating while chromatic aberrations are often obtained in case of slowly grown and thinner Au layers. A proper composition of the gold bath is fundamental to reduce galvanic effect as much as possible: effective complexing agents avoid Ni ions accumulation on the electrode surface changing the potential. In the worst situation, this unbalance of the Ni ion concentration in the bath and the difference in the metal ion concentration within the electrolyte result in the formation of concentration cell corrosion. In a condition of connected pads, the smallest ones may act as anodic sites subjected to Ni over-dissolution affecting component solderability.[18] Gold baths used for ENIG process typically involve different chelating agents, necessary to accelerating Ni ions dissolution, and gold-based salts as Au ions source. Clearly, chemicals can influence the kinetics of the reaction. Although nowadays baths based on different gold salts have been developed,[19–22] the most employed Au source, due to the bath stability and superior performances of the obtained coating, is still the potassium dicyanoaurate(I) $KAu(CN)_2$ salt.[23] Regarding the NiP chelating agents, the most used is Ethylenedyaminetetraacetic Acid (EDTA): in fact, once EDTA is dissolved in the electrolyte containing Ni ions, Ni-EDTA complexes are easily formed. Referring to the dissociation constant of EDTA at different pH,[24] and considering the pH value typically used in immersion processes, $EDTA^{4-}$ form is expected to be the dominant specie, chelating Ni^{2+} cations forming a five-coordinated complex $NiEDTA^{2-}$.[17,25,26] Another chelating agent typically used in the gold solution is citric acid which easily deprotonates in the solution forming a complex with Ni^{2+} cations like $NiCit^-$ or $NiCit_2^{4-}$depending on the pH of the solution.[17,26–28] Basing on the above considerations, in this paper we provide a comprehensive understanding of the mechanisms involved in the ENIG process, adopting an innovative approach coupling Raman in situ analysis and electroanalytical methods. In particular, the well-known issue of copper contamination in Au deposit was investigated, giving an insight to its origin and relation to the impact on final properties of the electronic components.

Material and Methods

Bath and electrodes preparation.—The effects of the ENIG process were studied in terms of NiP corrosion from the electrochemical and morphological point of view. The samples used were 40 × 10 × 0.35 mm copper plates, covered by a medium phosphorus (7% P by weight) electroless nickel deposit. Before the characterization, standard pre-treatment for cleaning and activation has been carried out:

- Samples degreasing by sonication in acetone for 5 min;
- Etching in 15 wt% H_2SO_4, 3 wt% H_2O_2 aqueous solution for 1 min;
- Surface activation by immersion in 2 g l^{-1} of palladium chloride and 35 wt% of HCl (1:2 ratio).

After these steps, the electroless NiP plating has been performed using the commercial Tecnoplate® solution at 85 °C for 25 min in order to obtain a 4–5 μm EN layer. Samples were then rinsed in deionized water and directly immersed into the electrolyte to be electrochemically tested. The immersion gold step was carried out for 10 min. Three different electrolytes, used for the electrochemical characterization, were prepared: 0.086 M EDTA based electrolyte (EDTA), 0.052 M citric acid based electrolyte (CA), mixture of them (EDTA/CA) and final immersion gold plating solution (IG). Electrolytes chemical composition and process parameters are shown in Table SI (available online at stacks.iop.org/JES/167/082507/mmedia).

Electrochemical characterization.—Electrochemical measurements have been carried out using AMEL2550 potentiostat/galvanostat with VApeak software. For both open circuit potential (OCP) and linear sweep voltammetry (LSV) measurements, exposed area for NiP substrates was of 2 × 1 cm^2. V_{OC} was recorded for 600 s at 85 °C and 250 rpm, using a two electrodes cell where electroless NiP substrate is employed as working electrode and Ag/AgCl (3 M KCl) as reference electrode. Potentiodynamic detections have been carried out in a three-electrodes cells, using electroless NiP as working electrode, Ag/AgCl (3 M KCl) as reference electrode and Elgard® Ru-oxides MMO net as counter electrode. Potentiodynamic measures were performed in a potential windows of (−0.5; −0.1) V, (−0.45; −0.1) V and (−0.6; −0.1) V for EDTA, citric acid and IG bath without gold salts based electrolytes respectively. The scan rate parameter was kept constant at 1 mV s^{-1} for all experiments.

In situ Raman spectroscopy.—Raman spectra were collected by means of LABRAM HR 800 UV HORIBA JOBIN YVON Argon ions LASER with 200× magnification. The argon ions laser provided the excitation at 785 nm and the power delivered to the samples was equal to 10 mW.

AFM and FE-SEM.—Surface morphology was analyzed by atomic force microscopy in contact mode. The AFM images were taken from eight samples, four for IG contaminated bath and four for IG Cu free bath, at different immersion times (t_i) i.e. 5 s, 20 s, 60 s and 180 s. Coatings morphology was characterized using Zeiss SUPRA 40 field emission scanning electron microscope (FE-SEM) with in-lens detector and energy dispersive spectroscopy (EDS).

Results and Discussion

ENIG process can be assumed as a controlled corrosion process, driven by the different nobility of involved metals i.e. Au and Ni, because galvanic displacement reaction occurs on NiP surface during the Au deposition. Since charge-transfer reactions are involved, different electroanalytical approaches can be applied to understand the role of different chelating agent on Ni dissolution during the process as well as the behavior of NiP surface in the chelate-containing solutions. Equilibrium potential and current trends have been investigated, respectively, by Open Circuit Potential (Voc) and Linear Sweep Voltammetry (LSV) measurements for NiP electrode immersed in different electrolyte solutions (see Table SI in supporting information (SI)). In Figs. 1a and 1b V_{OC} and LSV plots are respectively shown for EDTA-based solution (EDTA), Citric-based solution (CA) and mixture of them (EDTA/CA). The V_{OC} curves for NiP electrode are shown in Fig. 1a. The immersion potential of NiP in solution increased in the order EDTA < EDTA/CA w/o Au salt <CA. Opposite to EDTA (V_{OC}

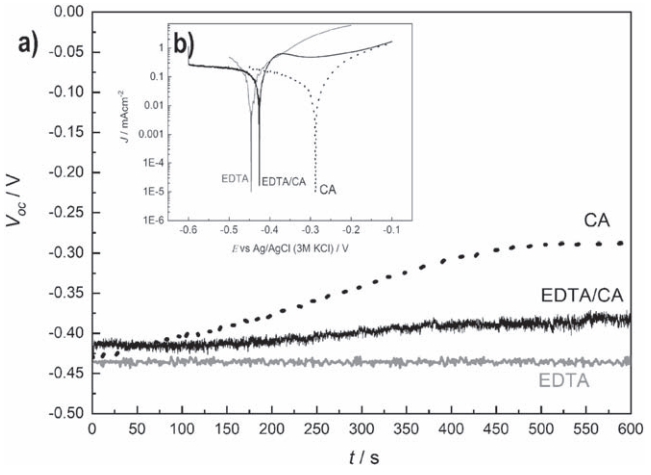

Figure 1. (a) Open circuit measurement and (b) LSV of NiP in 0.086 M EDTA electrolyte (gray line), 0.052 M CA electrolyte (dotted black line) and EDTA/CA electrolyte (black line).

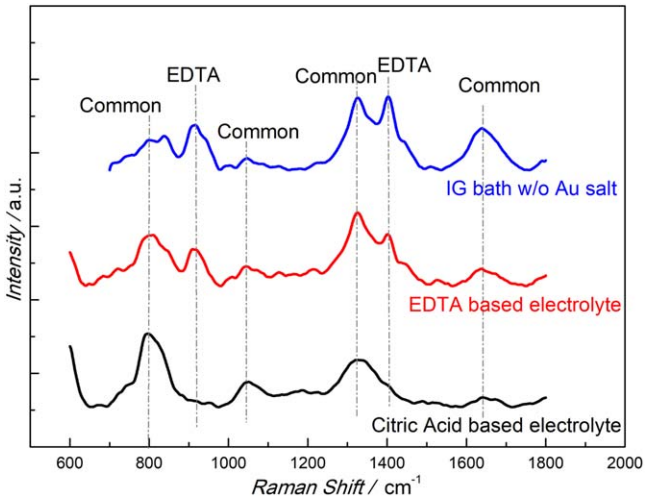

Figure 2. In situ Raman spectra collected in the carboxylic group frequencies. From the bottom: CA; EDTA and EDTA/CA electrolytes.

−0.436 V), immersion potential in CA-based solution was not constant during time but increased reaching a plateau value (V_{OC} −0.312 V). For the EDTA/CA electrolyte, where complexing agents were mixed, the immersion potential value (V_{OC} −0.390 V) was very similar to that of EDTA. However, considering only very short interval after NiP immersion, V_{OC} in CA solution is closed to EDTA one. As a consequence, the increasing potential vs time could suggest a role of CA in Ni complexation only at the very early stage of the reaction, while for longer time EDTA is the dominating chelating agent promoting NiP dissolution. This hypothesis was confirmed by LSV measurements, as shown in Fig. 1b: polarization of NiP in EDTA solution resulted in the most negative equilibrium potential (−0.446 V), similar to EDTA/CA mixture (−0.426 V), while a much less negative equilibrium potential was recorded for CA solution (−0.228 V). Furthermore, CA decreased the entire process current density for high overpotential values. Considering a practical working potential windows from −0.35 V to −0.55 V, CA was almost irrelevant respect to Ni dissolution, working mainly as pH buffering agent. In order to confirm the electrochemical results, to monitor the process evolution in time and to have a deep understanding of adsorption phenomena on NiP and Au surface during dissolution and deposition process, an innovative study was performed through Raman in situ spectroscopy. Spectra were collected at the proceeding of the process in different electrolytes. In Fig. 2 Raman spectra of EDTA, CA and EDTA/CA solutions are presented. The common features of the EDTA and citric acid molecules, mainly the carboxylate groups and carbon skeleton, resulted in the appearance of some common bands within the wavenumber window taken into consideration (600–1800 cm^{-1}) and summarized in Table I.[29,30] The broad bands at 793 cm^{-1} and 913 cm^{-1} could be assigned, respectively, to the asymmetric and out of plane COO^- deformation of the carboxylates. However, the latter was much more likely associated to the signal from the skeleton C–C vibration because of the absence of any absorption peak by the citric acid solution in the 890–950 cm^{-1} region. As already reported by M. A. Elbagermi et al.,[31] the C–C stretching in citric acid, usually centered at 936–940 cm^{-1}, disappeared in aqueous solution at mild acidic pH. The medium intensity peak at 1040 cm^{-1} was unidentified but it could be likely related to the carboxylate vibration or CH_2 stretching frequency, being a common feature of the three electrolytes. In the region 1000–1225 cm^{-1}, it was possible to observe an almost flat signal from citric acid solution, compared to the weak multiple bands from both EDTA and IG solutions. This evidence was consistent with the relatively low-sensitive Raman C–N stretching vibrations peculiar of this region, absent in citric acid. At higher wavenumber, it was possible to observe the main intensity

Table I. Main Raman bands and intensities of the three electrolytes systems in the carboxylic group frequencies.

Peak Position [cm^{-1}]	EDTA	CA	EDTA/CA
793	(s) [b]	(s)	(s)
915–950	(s)	—	(vs) [a]
1040	(m) [c]	(m)	(m)
1080, 1125, 1215	(w) [d]	—	(w)
1326	(vs)	(vs)	(vs)
1400	(vs)	(vw) [e]	(vs)
1447	(m)	—	(s)
1637	(m)	(m)	(s)

a) vs = very strong, b) s = strong, c) m = medium, d) w = weak, e) vw: very weak.

peaks of the spectra: the sharp peak at 1326 cm^{-1} was due to CH_2 twist and/or CO stretching, while the carboxylate symmetric group vibration strongly absorbed at 1400 cm^{-1} and the combination of CH_2CO deformation and CH_2 vibration could result in the medium-strong peak at 1447 cm^{-1}. The most important fingerprint for our purpose was the band raising at 1630 cm^{-1}, related to the asymmetric COO^- group vibration. As reported by A.A. McConnell and other authors,[32–36] the asymmetric stretching vibrations of the various types of COO^- group found in EDTA complexes have been observed to vary systematically with the nature of the group:

(i) ν_{as} COOH, above 1700 cm^{-1}: free carboxyl;
(ii) ν_{as} COOH, 1690–1660 cm^{-1}: co-coordinated carboxy1;
(iii) ν_{as} COO^-, 1660-l 620 cm^{-1}: covalently bonded carboxylate;
(iv) ν_{as} COO^-, 1620–1580 cm^{-1}: ionic carboxylate, either free or ionically bonded;
(v) ν_{as} COO^-, 1590–1560 cm^{-1}: bridging bi-dentate carboxylate.

Here, the 1630 cm^{-1} band indicates the ionized COO^- covalently bonded to water molecules by H-bonding. As general trend, from the intensity of the peaks, it was also possible to notice that EDTA seemed to result in a greater contribution to the IG bath Raman spectrum than citric acid. Adsorption phenomena for involved complexing agents have been evaluated during time as the Au galvanic reaction proceeds. Raman spectra of NiP in the complete IG bath were collected for a different time (see Fig. S1 for the results). Three main features have to be high lightened: (i) the characteristic frequencies, discussed before, corresponding to each complexing agent decreased in intensity during time due to the gold layer growth, (ii) the intensity reduction was much greater in the 1000–1225 cm^{-1} region, where C–N absorbs, (iii) the ν_{as} COO^- shifts at 1598 cm^{-1}. The lowering in the intensity can be explained by the complexation of EDTA and citric acid with Ni^{2+} (by the formation of Ni^{2+} complexes $NiEDTA^{2-}$ and $NiCit^-/NiCit_2^{4-}$), that occurred on the electrode surface and the progressive desorption of the complexes resulting in the decrease of the relative concentration of adsorbed species. In particular, the evident lowering in the C–N stretching region could be assigned to the major role and faster kinetics of EDTA complexation and desorption, with respect to citric acid, in the early stage of the ENIG process, consistently with the electrochemical results. Moreover, the red shift of the ν_{as} COO^- from 1630 cm^{-1} to 1598 cm^{-1} was a clear fingerprint of the protonation of the carboxylate and subsequent formation of complexes $NiEDTA^{2-}$ and $NiCit^-/NiCit_2^{4-}$ (Ni^{2+} complexes).[36–38] In this series of experiments, a peak typical of H_2SO_4 used for pH adjustment is also present at 980 cm^{-1}. The entire process involving gold species was also characterized by means of electrochemical and spectroscopic techniques focusing in particular on gold deposition mechanism for both pure IG solution and Cu^{2+} polluted one, i.e. with addition of 10 ppm Cu^{2+} to simulate the copper pollution in the

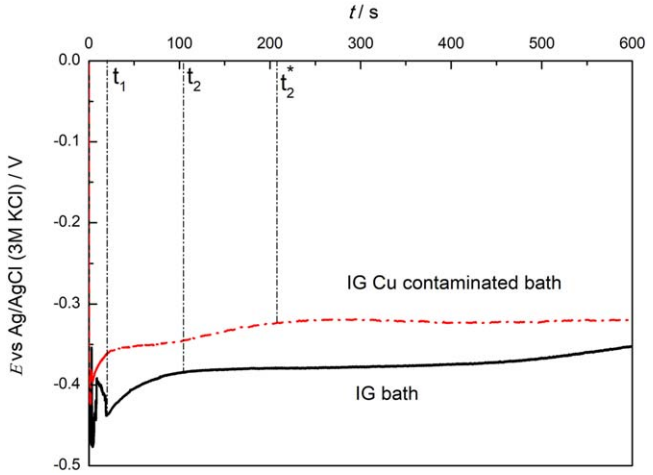

Figure 3. Open circuit potential measurement of NiP in IG bath and IG-Cu bath for the whole immersion process.

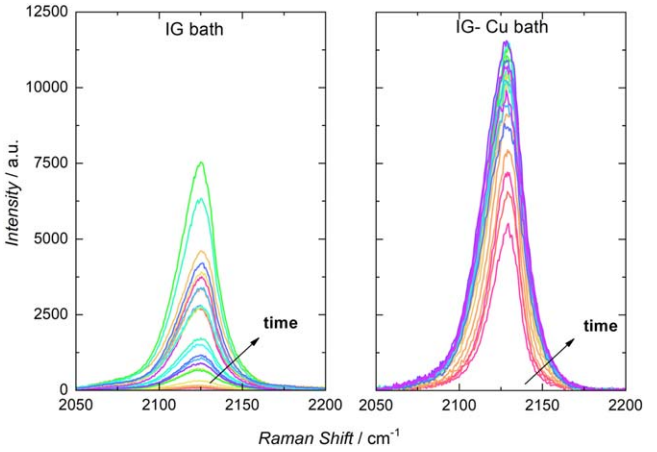

Figure 5. In situ Raman spectra collected each 30 s in the Me–C≡N stretching frequency range for EN in IG electrolyte on the left and IG-Cu bath on the right at different times.

industrial plating processes. The V_{OC} of NiP in IG bath, with and without Cu contamination (IG-Cu), showed a peculiar behavior that can be interpreted according to H. Liu et al.[39]: the immersion gold process could be divided into three phases: (i) $t < t_1$, (ii) $t_1 < t < t_2$ and (iii) $t > t_2$ respectively. After the very first time $t < t_1$, where the electrode potential dropped due to the adsorption of both $Au(CN)_2^-$ and other negative species like EDTA and citrate ions, the potential gradually shifted to more positive values for $t_1 < t < t_2$, time in which the gold deposition effectively started inducing the progressive Ni ions displacement by the gold layer. For higher deposition times, $t > t_2$, the Au layer growth on NiP substrate stabilized the potential at −0.428 V, reaching a plateau. As already demonstrated in several studies,[6,40] the gold deposition does not stop but it continues for a long time after the gold deposit has already built up due to the presence of porosity of the growing more noble metal layer: the porous gold structure allows more noble ions to penetrate and to get in contact with the nickel surface resulting in continuous deposition at the plateau potential. Analyzing the V_{OC} characteristic curve (Fig. 3) for IG bath, the onset of gold deposition time (t_1) was equal to 19.2 s while the time for effective gold film buildup on nickel substrate (t_2) was equal to 105.8 s. A schematic representation of different stages of deposition during time is shown in Fig. 4. The gold layer thickness measured with X-ray fluorescence in these conditions was equal to 61 nm, corresponding to a deposition rate of 0.1 nm s^{-1}. Comparing these results with those obtained from IG-Cu solution shown in the same figure, the presence of Cu ions induced the V_{OC} curve shifting trough positive direction by about 55 mV suggesting that some copper complexes could be adsorbed on the electrode surface. In addition, characteristic times for polluted solution were completely different: the gold deposition effectively started after 4 s, reducing the onset of Au deposition by a factor of five, and the gold deposition proceeded longer than IG bath until 209.6 s before reaching the plateau potential at −0.322 V. Considering the electrochemical behavior, the plating rate for the IG-Cu case should be lower than the pure IG bath. However, the gold layer thickness measured with X-ray fluorescence in this case was equal to 145 nm corresponding to a plating rate of 0.242 nm s^{-1}, about two times higher than the previous case. In order to understand the effects of Cu contamination on chemical species adsorbed on NiP electrode while ENIG process proceeds, in situ Raman spectroscopy was used. As soon as the NiP sample was in contact with IG solution, $Au(CN)_2^-$ complexes were immediately adsorbed on the electrode surface. As it is possible to see from Fig. S2, three characteristic vibration modes could be identified[41–46]:

(i) Extramolecular Au–C stretching at 297 cm^{-1};
(ii) Au−C≡N bending at 383 cm^{-1};
(iii) Au−C≡N stretching at 2124 cm^{-1}.

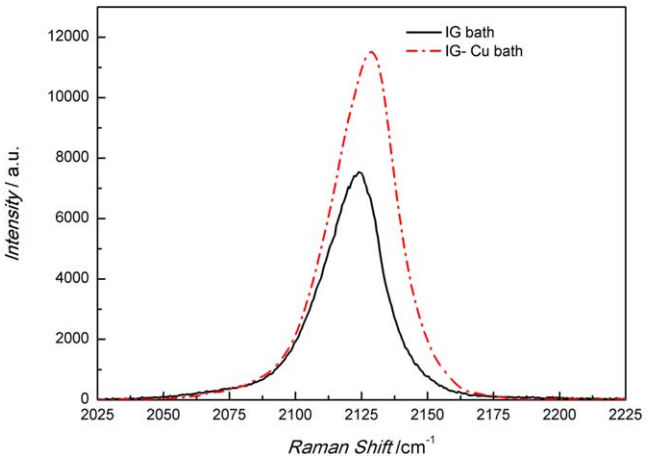

Figure 6. In situ Raman spectra collected at 600 s of NiP substrate in IG electrolyte and IG-Cu electrolyte.

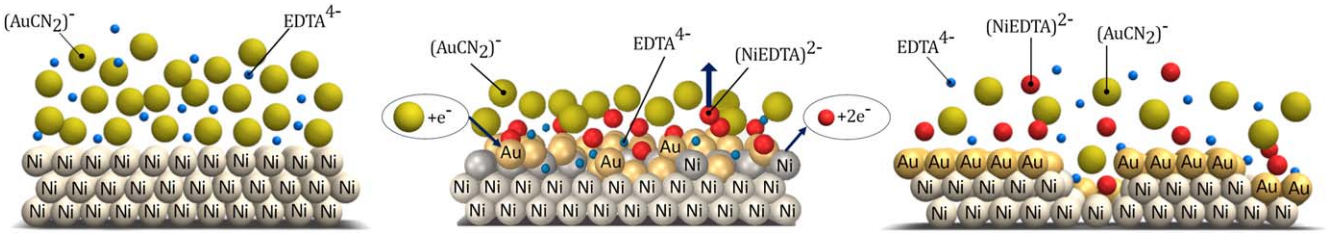

Figure 4. Schematic representation of different stages of immersion gold plating at increasing time of immersion.

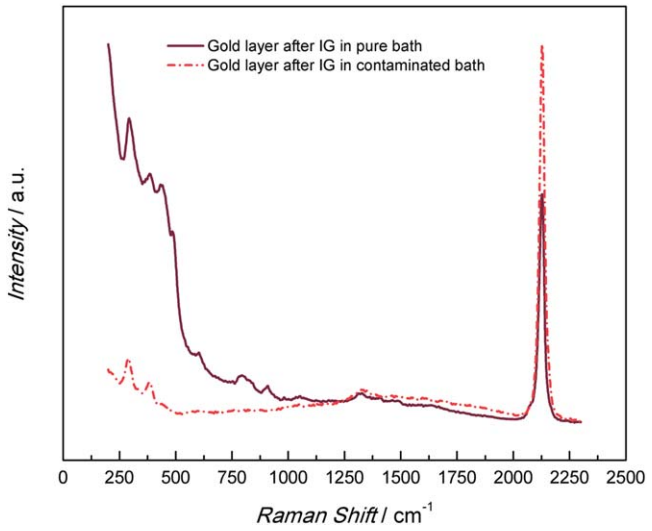

Figure 7. Raman spectra collected on gold layer at the end of the immersion plating after rinsing and air drying for IG pure bath and for IG-Cu bath.

Furthermore, in the wavenumber window from 600 to 1200 cm^{-1} vibration modes corresponding to adsorption of complexing agents previously discussed were still present. In order to understand the adsorbed species evolution and to characterize them during the entire immersion gold process, a series of temporal mapping experiments using both electrolytes have been carried out: spectra were collected at each 30 s keeping constant process parameters, i.e. temperature and pH, for both electrolytes focusing only on the Me−C≡N stretching vibration frequency, used in this case as indicator of cyanide complexes adsorption. From results, shown in Fig. 5, it is possible to evince that contamination of IG solution induced Me–C≡N vibration variation. The intensity of the peak increased proportionally during time for both solution although it was about two orders of magnitude higher in case of Cu contaminated solution since the beginning of the process, symptomatic of a faster growth rate of the gold layer. At longer process time, about 300 s, the signal stopped growing and intensity variation corresponding to surface-enhanced Raman scattering (SERS)[47] effect could be noticed. In addition, considering the two last spectra at the end of the process (Fig. 6), collected while samples were still immersed in the solution, the characteristic frequency corresponding to Me−C≡N stretching mode blue-shifted from f. 2124 cm^{-1} for IG bath to 2128 cm^{-1} in case of IG-Cu bath. Both higher intensity and wave number shifting of ν_{CN} peak in case of Cu presence could be ascribed to the adsorption of copper cyanide complexes on the electrode surface competitive with the $Au(CN)_2^-$ complex adsorption, whose competitive adsorption has been already demonstrated for other substrates.[48–51] Although Cu was dissolved as Cu^{2+}, it could pass from cuprous to cupric form in presence of cyanide ions. Considering the dissociation of hydrogen cyanide in aqueous solution and the pH of the electrolyte, copper(I) complexes were present as a mixture of $Cu(CN)_2^-$ and $Cu(CN)_3^{2-}$.[50–52] Although Cu(II) ions could be also complexed by EDTA, the stability constant of the complex $Cu(EDTA^{4-})$ in the same condition is lower and Cu cyanide complexes are the dominating species.[53,54] Furthermore, in situ-Raman measurements on samples immersed in IG plating solution and IG-Cu bath for 600 s, rinsed several times and air-dried, revealed that cyanides peaks with different intensity and characteristic frequency previously identified were still present (Fig. 7). This residual adsorption of cyanide groups on the electrode surface at the end of process could induce corrosion phenomena for the metallic layer in the long term.[55] The different chemical adsorption phenomena observed in case of Cu pollution combined with electrochemical results suggested that contamination could induce gold layer morphological changes. In order to confirm that, samples treated at different immersion times (t_i), i.e. 5 s, 20 s, 60 s and 180 s, in the two electrolytes have been analyzed using field emission scanning electron microscopy. Looking at Fig. 8, it is possible to see that the dimension of nuclei in case of Cu free solution was smaller with respect to the Cu contaminated case. While the immersion gold deposition proceeded, the gold morphology was substantially different in the two cases: the gold layer seemed to grow planarly

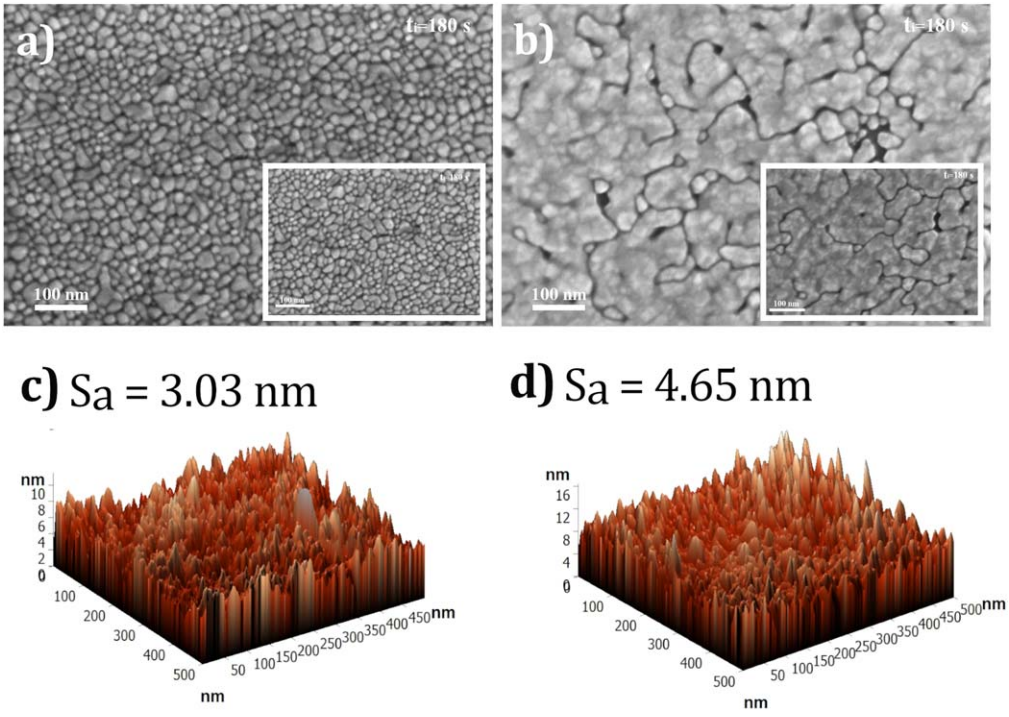

Figure 8. (a) SEM images after 180 s of immersion time of EN substrate in IG solution and (b) in IG-Cu bath; (c) AFM measurements on 500 nm × 500 nm surface for EN substrate after 180 s of immersion in IG solution and (d) in IG-Cu bath.

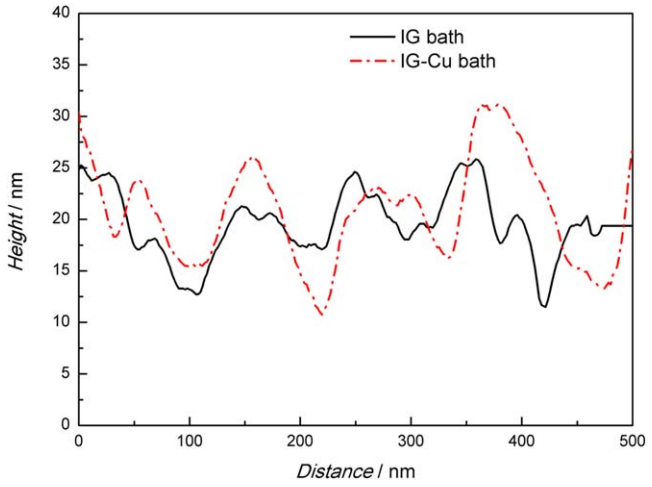

Figure 9. Roughness profiles for samples immersed for 180 s into IG bath and IG copper contaminated one.

in case of pure IG electrolyte, while in case of IG-Cu solution larger clusters were present and the gold deposit was characterized by more disordered three-dimensional structure (Fig. 8b). This could be explained considering similar effects of metallic impurities on electro-kinetic parameters in gold plating: it was demonstrated that metallic ions with low exchange current density for hydrogen evolution and relatively high exchange current density for the metal redox reaction, e.g. Cu and Ag as far as Tl, can promote the growth of large clusters maintaining a 2D planar growth. These elements at the surface can shift the cathodic voltage toward to less negative values during the deposition, reducing the inhibition condition thus favoring the interaction of the complexing agent with the surface.[56] The gold layer evolution in terms of nucleation and growth at different immersion times is available in Figs. S3 and S4. The different gold morphology was confirmed also by AFM analyses carried out on the same samples on a surface of 500 nm × 500 nm. Results are shown in Fig. S6 where the effectively more porous and rougher surface in case of polluted solution could be observed. The root mean square height (S_q) value in case of pure IG electrolyte was equal to 3.54 nm, while it was equal to 5.99 nm in case of polluted solution. Furthermore, looking at Fig. 9 in which profiles roughness for samples immersed in the two different solution for 180 s are shown, it is easy to notice that the distance between peaks and valleys was higher in case of contaminated solution. The roughness evolution study at different times of immersion, from 5 s to 180 s, both in IG and IG-Cu solutions is shown in Figs. S5 and S6. The evaluation of gold layer performance from the solderability point of view has been done using two different samples plated IG bath and IG-Cu bath according to NF-A-89 400 standard using a Sn based solder paste. Results are reported in Fig. 10 and, according to the standard, the test can be considered passed if the solder wetting curve passes through the highlighted area into the graph: the failure of the test in case of Cu contaminated sample could be ascribed to the co-deposition of copper into the metal layer which quickly oxidizes making the component unsolderable.

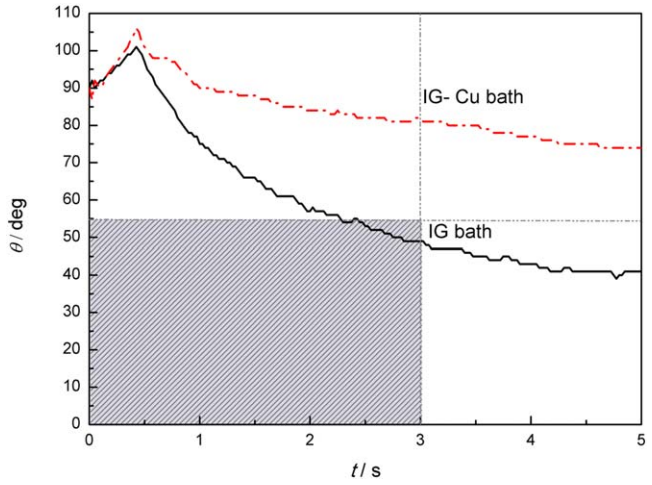

Figure 10. Solderability test according to NF-A-89 400 for gold layer obtained with IG bath (line) and IG-Cu bath (dot line).

Conclusions

Electrochemical and spectroscopic results of different Ni ions complexing agents involved in the ENIG process revealed that EDTA is the most effective complexing agent: from V_{OC} and LSV experiments emerged that the electrochemical behavior of NiP in the complete solution is EDTA-dominated while the citric acid affects the current density of the process only at very high anodic overpotentials. In case of complete immersion gold electrolytes, in situ Raman investigations showed that intensity of vibration modes associated with metal-cyanide bonds increased proportionally with time; after 300 s SERS effect could be noticed for both electrolytes. Considering the pollution effect, both the reduction of the gold deposition onset and the V_{OC} positive shifting induced by copper contamination, suggest that Cu complexes are adsorbed on the metal surface while the galvanic displacement proceeds. This was confirmed by in situ Raman spectroscopy experiments: the pollution increased the intensity of peaks corresponding to cyanides vibration modes since the beginning of the process, causing the blue shift of the frequency corresponding to Me−C≡N stretching vibration from 2124 cm^{-1} to 2128 cm^{-1}. These evidences indicate that a $Cu(CN)_2^-$ and/or $Cu(CN)_3^{2-}$ complexes, competitive with the $Au(CN)_2^-$ complex adsorption, can be present at the substrate surface inducing both morphological and topographical variations, affecting the solderability of the component due to copper oxidation phenomena.

Funding

This research did not receive any specific grant from funding agencies in the public, commercial, or not-for-profit sectors.

ORCID

Alessandra Accogli https://orcid.org/0000-0001-7154-9349
Eugenio Gibertini https://orcid.org/0000-0002-2610-5500
Gabriele Panzeri https://orcid.org/0000-0003-3460-7786
Andrea Lucotti https://orcid.org/0000-0003-2148-1408
Luca Magagnin https://orcid.org/0000-0001-5553-6441

References

1. R. Khandpur, *Printed Circuit Boards: Design, Fabrication, Assembly and Testing* (Tata McGaw-Hill Education, India) (2005).
2. National Academy of Science, *Linkages: Manufacturing Trends in Electronics Interconnection Technology* (National Academies Press, Washington, DC) p. 1 (2005).
3. A. Canal Marques, J. M. Cabrera, and C. De Fraga Malfatti, *J. Environ. Manage.*, **131**, 298 (2013).
4. K. Zeng, R. Stierman, D. Abbott, and M. Murtuza, *Thermal and Thermomechanical Proceedings 10th Intersociety Conference on Phenomena in Electronics Systems, 2006. ITHERM* (IEEE), Piscataway, NJ p. 1111 (2006), http://ieeexplore.ieee.org/document/1645469/.
5. G. Mallory and J. Hajdu, *Electroless Plating: Fundamentals and Applications* (AESF, Orlando, Florida) (1990).
6. S. S. Djokić and P. L. Cavallotti, *Electrodeposition Theory and Practice* (Springer Science & Business Media, New York) p. 251 (2010).
7. Y. Okinaka and T. Osaka, *Advances in Electrochemical Science and Engineering 3* (VCH Publishers, New York) p. 55 (2008).
8. S. S. Djokić and L. Magagnin, *Electrodeposition and Surface Finishing: Fundamental and Application* (Springer, Berlin) p. 341 (2014).
9. T. Osaka, T. Misato, J. Sato, H. Akiya, T. Homma, M. Kato, Y. Okinaka, and O. Yoshioka, *Electrochem. Soc.*, **147**, 1059 (2000).

10. N Biunno and M. Barbetta, *Surface Finishes Forum Conf. Proc. IPC Printed Circuits Expo1999, paper (SMTA)*, **99**, 14 (1999).
11. P. Snugovsky, P. Arrowsmith, and M. Romansky, *J. Electron. Mater.*, **30**, 1262 (2001).
12. D. J. Lee and H. S. Lee, *Microelectron. Reliab.*, **46**, 1119 (2006).
13. R. W. M. Kwok, K. C. M. Chan, and M. W. Bayes, *Circuit World*, **30**, 37 (2004).
14. F. D. B. Houghton, *Assembly Proceeding of ICP Works*, **99**, 23 (1999).
15. H. Lee, J. Jung, C. Heo, C. Kim, J. H. Lee, and Y. Kim, *J. Electron. Mater.*, **47**, 5158 (2018).
16. R. Ramanauskas, A. Selskis, J. Juodkazyte, and V. Jasulaitiene, *Circuit World*, **39**, 124 (2013).
17. Y. S. Won, S. S. Park, J. Lee, J. Y. Kim, and S. J. Lee, *Appl. Surf. Sci.*, **257**, 56 (2010).
18. B. K. Kim, S. J. Lee, J. Y. Kim, K. Y. Ji, Y. J. Yoon, M. Y. Kim, S. H. Park, and J. S. Yoo, *J. Electron. Mater.*, **37**, 527 (2008).
19. Y. Okinaka and M. Hoshino, *Gold Bull.*, **31**, 3 (1998).
20. Y. Wang, H. Liu, S. Bi, M. He, C. Wang, and L. Cao, *RSC Adv.*, **6**, 9656 (2016).
21. J. Sato, M. Kato, H. Otani, T. Homma, Y. Okinaka, and T. Osaka, *J. Electrochem. Soc.*, **149** (2002).
22. Y. Wang, X. Cao, W. Wang, N. Mitsuzak, and Z. Chen, *Surf. Coatings Technol.*, **265**, 62 (2015).
23. T. N. Vorobyova, S. K. Poznyak, A. A. Rimskaya, and O. N. Vrublevskaya, *Surf. Coatings Technol.*, **176**, 327 (2003).
24. M. Chen and R. S. Reid, *Can. J. Chem.*, **71**, 763 (1993).
25. B. Nowack and L. Sigg, *J. Colloid Interface Sci.*, **177**, 106 (1996).
26. Z. Wang, J. Reibenspies, and A. E. Martell, *Inorg. Chem.*, **36**, 629 (1997).
27. G. R. Hedwig, J. R. Liddle, and R. D. Reeves, *Aust. J. Chem.*, **33**, 1685 (1980).
28. O. Y. Zelenin, *Russ. J. Coord. Chem. Khimiya*, **33**, 346 (2007).
29. G. Socrates, *Infrared and Raman Characteristic Group Frequencies* (Wiley & Sons LTD, Chichester) (2001).
30. K. Krishnan and R. A. Plane, *J. Am. Chem. Soc.*, **90**, 3195 (1968).
31. M. A. Elbagermi, A. I. Alajtal, H. G. M. Edwards, G. H. Azimi, K. D. Verma, and I. J. Scowen, *J. Appl. Chem. Sci. Int. 2(1)1–11,2015*, **2**, 1 (2015).
32. A. A. McConnell, R. H. Nuttall, and D. M. Stalker, *Talanta*, **25**, 425 (1978).
33. K. Nakamoto, *Infrared Spectra of Inorganic and Coordination Compounds* (Wiley, New York, NY) (1963).
34. K. Nakamoto, *Handbook of Vibrational Spectroscopy*, ed. P. R. Griffiths (John Wiley & Sons, Ltd, Chichester, UK) (2006).
35. D. T. Sawyer and J. E. Tackett, *J. Am. Chem. Soc.*, **85**, 314 (1963).
36. E. Faulques, D. L. Perry, S. Lott, J. Zubkowski, and E. Valente, *Spectrochim. Acta Part A Mol. Biomol. Spectrosc.*, **54**, 869 (1998).
37. R. H. Nuttall and D. M. Stalker, *J. Chem. Soc. Dalt. Trans.*, **19**, 1884 (1977).
38. R. H. Nuttall and D. M. Stalker, *Inorg. Nucl. Chem. Letters*, **12**, 639 (1976).
39. H. Liu, N. Li, S. Bi, and D. Li, *J. Electrochem. Soc.*, **154**, D662 (2007).
40. S. S. Djokić, *J. Electrochem. Soc.*, **143**, 1300 (1996).
41. B. Bozzini and A. Fanigliulo, *J. Appl. Electrochem.*, **32**, 1043 (2002).
42. B. Bozzini, L. D'Urzo, C. Mele, B. Busson, and A. Tadjeddine, *Trans. IMF*, **88**, 130 (2010).
43. F. Huerta, C. Mele, B. Bozzini, and E. Morallón, *J. Electroanal. Chem.*, **569**, 53 (2004).
44. J. M. Smith, L. H. Jones, I. K. Kressin, and R. A. Penneman, *Inorg. Chemystry*, **4**, 369 (1965).
45. L. H. Jones and J. M. Smith, *J. Chem. Phys.*, **41**, 2507 (1964).
46. L. H. Jones, *J. Chem. Phys.*, **43**, 594 (1965).
47. A. Campion and P. Kambhampati, *Chem. Soc. Rev.*, **27**, 241 (1998).
48. X. Dai, M. I. Jeffrey, and P. L. Breuer, *Hydrometallurgy*, **101**, 99 (2010).
49. X. Dai, A. Simons, and P. Breuer, *Miner. Eng.*, **25**, 1 (2012).
50. J. H. Kyle and G. Hefter, *Hydrometallurgy*, **154**, 78 (2015).
51. G. C. Lukey, J. S. J. Van Deventer, S. T. Huntington, R. L. Chowdhury, and D. C. Shallcross, *Hydrometallurgy*, **53**, 233 (1999).
52. J. Lu, D. Dreisinger, and W. Cooper, *Hydrometallurgy*, **66**, 23 (2002).
53. N. Tanaka, M. Kamada, and T. Murayama, *Bull. Chem. Soc. Jpn.*, **31**, 895 (1958).
54. M. T. Beck, *Pure Appl. Chem.*, **59**, 1703 (1987).
55. K. Cimatu and S. Baldelli, *J. Am. Chem. Soc.*, **130**, 8030 (2008).
56. P. L. Cavallotti, P. Cojocaru, and L. Magagnin, *Trans. IMF*, **90**, 246 (2012).